Published in final edited form as:
Int J Med Robot. 2011 June ; 7(2): 138–147. doi:10.1002/rcs.381.

Does Needle Rotation Improve Lesion Targeting?

Shadi Badaan, MD[1], **Doru Petrisor, PhD**[1], **Chunwoo Kim**[1], **Pierre Mozer, MD PhD**[1], **Dumitru Mazilu, PhD**[1], **Lucian Gruionu, PhD**[1], **Alex Patriciu, PhD**[1], **Kevin Cleary, PhD**[2], and **Dan Stoianovici, PhD**[1]

[1]Robotics Laboratory, Department of Urology, Johns Hopkins Medicine, Baltimore, MD

[2]Departments of Radiology and Surgery, Children's National Medical Center, Washington, DC, http://urobotics.urology.jhu.edu/

Abstract

Background—Image-guided robots are manipulators that operate based on medical images. Perhaps the most common class of image-guided robots are robots for needle interventions. Typically, these robots actively position and/or orient a needle guide, but needle insertion is still done by the physician. While this arrangement may have safety advantages and keep the physician in control of needle insertion, actuated needle drivers can incorporate other useful features.

Methods—We first present a new needle driver that can actively insert and rotate a needle. With this device we investigate the use of needle rotation in controlled in-vitro experiments performed with a specially developed revolving needle driver.

Results—These experiments show that needle rotation can improve targeting and may reduce errors by as much as 70%.

Conclusion—The new needle driver provides a unique kinematic architecture that enables insertion with a compact mechanism. Perhaps the most interesting conclusion of the study is that lesions of soft tissue organs may not be perfectly targeted with a needle without using special techniques, either manually or with a robotic device. The results of this study show that needle rotation may be an effective method of reducing targeting errors.

Introduction

The growing acceptance of minimally invasive treatments as an alternative to open surgery has created a demand for more accurate and precise surgical technologies. Medical robots are one technology that could contribute to this need.

Needle insertion is a commonly performed component of minimally invasive procedures and clinical interventions and is extensively used for diagnostic and therapeutic purposes [1]. These procedures include percutaneous organ or tumor biopsy, cryo or radiofrequency needle insertion for tumor ablative therapies such as percutaneous liver tumor ablation, and brachytherapy needle insertion for uterine or prostate cancer treatment. Other needle-based procedures include vessel needle access as the initial part of all endovascular procedures, and percutaneous needle insertion for drainage treatment such as percutaneous cholecystostomy tube insertion for gallbladder decompression or as the initial step in more complicated procedures such as percutaneous nephrolithotripsy.

Correspondence to: Dan Stoianovici PhD, JHBMC, Urology Robotics Laboratory, MFL-W115, 5200 Eastern Avenue, Baltimore, MD 21224, USA, Tel: 410-550-1980; dss@jhu.edu.

Substantial improvements have been made in this field from the time when technology limited physician's feedback to simple palpation of suspicious lesions for planning biopsy needle access. Improvements include refinements in needle technology such as optimizing thickness, point geometry, and triggering mechanisms; using advanced imaging modalities for guiding purposes; and ultimately incorporating medical robots to place the needle. These improvements made precise needle targeting feasible and more reliable, and continued work promises to further advance these technologies.

However, there are still technology challenges to be overcome, including problems related to needle bending, soft tissue deflection, and breath induced movements [2, 3], which influence the overall targeting accuracy. Needle delivery errors have a direct impact on the outcome of the procedure. Moreover, complications may also be related to needle misplacement. The common assumption is that the needle remains straight during insertion, yet this is not always the case, particularly with thinner needles. During insertion the needle is likely to encounter variable resistance as it crosses heterogeneous tissues [4]. The axial force of needle insertion is related to tissue characteristics and needle mechanical and geometric properties. For example in percutaneous kidney access the needle encounters a tougher layer of skin, softer muscle and fat, then easily passes the parenchyma, to finally "poke" the collecting system. Even though the main components of these forces are axial, tissue deflections may create lateral displacements and forces that cause needle bending and mis-targeting in both lateral and axial directions. Therefore, even if the needle is directly aimed at the target before the insertion, the needle may not hit it due to these factors.

Some investigators have proposed methods for modeling forces during insertion [4–6], representing force balance in a classic free-body diagram. Axial forces include the cutting force, friction force, and clamping force. The cutting force is assumed to be the force acting at the needle point while advancing the needle. Its magnitude is affected by the shape of the needle point and tissue characteristics. The friction force acts mainly along the needle shaft and is assumed to have Coulomb static, kinetic, and viscous friction components. A so-called "clamping" force is also considered for the wedging effort of the needle point to make room for its passage, the magnitude of this force being affected by the needle gauge. However, the variability and uncertainty of soft tissue properties along the needle path make it difficult to create realistic models and predictions of needle insertion. Nevertheless, this has been an area of active research [4, 7–9].

Other solutions have been proposed to improve targeting precision and accuracy, including the use of needles with a diamond point rather than a beveled point to minimize lateral drift, the use of high velocity insertion, rotary or linear oscillations, and needle rotation [7, 10–13]. The effect of needle geometry on insertion forces and needle bending was shown to be significant [4] and, as well-known by clinicians, beveled point needles drift laterally. Techniques have been introduced for overcoming the drift [10], including midway opposite rotation, needle rotation, and model-based rotation depending on tissue and needle properties. Needle steering methods have been proposed to overcome bending and soft tissue deflections by real-time needle control. These methods aim to reach the target while avoiding obstacles or critical structures along the needle path [14–17].

Experiments analyzing the influence of insertion speed revealed that speed typically increases axial forces and hence causes eventually more tissues deflection and target displacement [12]. However, it is likely that high-velocity insertions (needle "shooting") could potentially improve targeting [18–21]. In any case, during minimally invasive procedures quick insertions could be employed to minimize errors contributed by patient and physiological motion. Linear oscillation of the needle was found to minimize target displacement but led to added tissue damage [12]. Rotary oscillation at low frequency made

little difference; in fact this increased axial forces, which were directly related to target displacement.

However, continuous needle rotation may be beneficial. As shown in this paper and observed by others [13] continuous needle rotation lowers lateral needle deflection, which maintains the needle on a straighter path and reduces needle friction causing less soft tissue compression and target displacement. Our experiments are performed with a specially designed robot equipped with a custom needle driver, the Revolving Needle Driver (RND). The driver supports the needle from its barrel and head and can rotate the needle in a drill-like motion. Built-in force sensors are used to measure the forces exerted on the needle. The driver was designed to be used in conjunction with our AcuBot robot system [22] that was intended mainly for x-ray guided interventions and can be installed on computed tomography (CT) scanners.

Most image-guided robots position and orient a needle guide. The needle is then manually placed through the guide [23]. This approach has certain advantages such as keeping the physician in direct control of the needle, instrument simplicity, and perhaps facilitating regulatory approvals for clinical trials and use. However, the use of a fully actuated needle driver allows for fully automated robotic image-guided procedures as shown by others [13, 24–26] and presented herein.

In this paper we present a feature-rich needle driver and results of a set of in-vitro experiments to assess the influence of rotation on axial resistance forces and target displacement. The conclusions summarize the results and offer suggestions that could be instrumental with other devices as well as manual needle handling.

Methods

Revolving Needle Driver (RND) and Robotic System

The revolving needle driver (RND) has the main function of inserting and retracting a needle. The driver also presents other degrees of freedom (DOF) and auxiliary features. The RND could be used independently (handheld or supported by a positioning arm) or in conjunction with image-guided robots such as the AcuBot robot [22] developed in our laboratory. The AcuBot presents a bridge like structure that mounts over the table of a CT scanner and compact geometry near its distal end that enables it to fit within the bore of the scanner. The AcuBot base provides the RND with 5-DOF. The RND is supported by the RCM (Remote Center of Motion) module [27, 28], a passive positioning arm, a 3-DOF Cartesian positioning stage, and a bridge support over the table. Figure 1 shows the RND supported by the RCM and the AcuBot robot attached to its control cabinet when not in use.

The RCM is a 2-DOF robotic orientation module that orients the RND about two orthogonal directions (Rx and Rz) while maintaining the fixed location of the RCM point at the tip of the bottom nozzle point. In operation the tip of the needle is aligned with the bottom nozzle point and placed at the desired skin entry point. The RND presents two decoupled DOF for inserting the needle (Ty) and rotating it (Ry).

Needle Insertion Mechanism

Traditionally, translational motion is created with slider (prismatic, translational) joints. However, these mechanisms are commonly longer than their stroke which makes the driver taller than the needle it handles. This may create interference problems when operating in the compact space of a medical imager. The RND uses a novel compact mechanism to achieve quasi-linear motion with rotary joints. The kinematic diagram of the needle insertion mechanism is presented in Figure 2.

The mechanism consist of a crank P_1–P_2, the rod P_2–P_4, the pin (revolute) joints P_1, P_2, P_3, and the slider joint P_3. The pin and slider joints P_3 have normal intersecting axes. Near linear motion of the end point P_4 (needle head) along the axis Y is achieved by optimizing the size of the mechanism, where the optimum values (scalable) are shown in the figure. The direct kinematics of the mechanism, describing the position of the needle point P_5 in the *XYZ* coordinate system as a function of the crank angle *u*, is given in Equations 1:

$$y(u)=L_1\sin(u)\left(\frac{L_2}{(L_1\cos(u)-Z_1+Z_2)\sqrt{1+\frac{{L_1}^2\sin(u)^2}{(L_1\cos(u)-Z_1+Z_2)^2}}}-1\right)+Y_1-L_n$$

$$z(u)=L_1\cos(u)-\frac{L_2}{\sqrt{1+\frac{{L_1}^2\sin(u)^2}{(L_1\cos(u)-Z_1+Z_2)^2}}}+Z_2$$

(Equation 1)

The dependence of the *y* and *z* coordinates on the driving angle *u* is also shown in Figure 2. These show that the insertion motion is nearly linear with a small lateral displacement (< 0.5 mm). As shown later, the lateral displacement effect on the direction of the needle is further minimized by the needle guide of the nozzle.

Closed loop control of the crank angle *u* is performed with feedback from the motor encoder. A redundant encoder is used for safety purposes along with a watchdog circuit. The encoder is custom constructed with two optical sensors (Omron EE-SPX842) spaced to implement a quadrature encoder over the teeth of the final gear of the transmission chain (Berg PFA 94-80, 80 teeth).

The orientation of the rod P_2–P_4 changes when the needle is inserted. Therefore, a parallel motion mechanism is used to maintain the direction of the needle head during insertion, as shown in Figure 3. This mechanism uses two belts, connected between equal pair pulleys P_1–P_2 and P_2–P_4. Because the first pulley P_1 is connected to the base of the RND, the end pulley P_4 maintains the same orientation (parallel mechanism) independent of the position of the needle insertion mechanism. The head of the needle is driven by pulley P_4, which presents quasi-translational motion.

Needle Rotation and Release Mechanisms

The needle is spun from its head through a gear transmission as shown in Figure 4. The head of the needle is fitted with a gear that can be easily placed by hand. Needle adapters are used to accommodate commercial needles of various sizes (Cook DGB-18-15.0 needle shown). The nozzle of the driver is sized to match the gauge of the needle. A small size geared servomotor (Maxon Motor) is enclosed in the P_4 Body.

The needle driver can also release the needle on command. As shown in Figure 5, the needle is held with two grippers at the head of the needle and at the bottom through the nozzle. The head gripper revolves and inserts the needle while the nozzle guides its direction. Each gripper has two finger-like arms that clip (fasten) for holding and move outward for releasing the needle. Mounting the needle is done manually by closing the fingers, while the release is actuated by a common pneumatic command that simultaneously releases both finger mechanisms. An outward opening motion was provided so that the release action does not disturb the position of the needle but simply lets go.

For sterilization, the driver is covered with a sterile bag that also covers the other parts of the robotic arm. The two needle adapters and the two grippers are sterilized and disposable. The grippers pierce through the sterile bag and mount with eccentric locks.

Force Sensors

Two custom-built force sensors are part of the driver. One sensor measures the three force components exerted at the nozzle point. The other sensor measures the axial force of needle insertion using a custom torque sensor connected on the transmission chain of the insertion axis with full-bridge thin-beam load cells (Omega LCL-005). The nozzle sensor is custom built within the lower arm supporting the barrel gripper (Figure 6). Six stress concentration regions have been modeled for six identical strain gauges (HBM 1-LY13-3/120) to measure the corresponding stains. Their geometry was modeled using geometric element modeling methods in Pro/Engineer (Parametric Technology Corporation) so that the resulting strains fall within the measurement range of the strain gauges (0-50N forces were simulated at the nozzle point about the *XYZ* directions).

The mapping K of the six-dimensional (6D) strain space X and the 3D Cartesian space of forces F is chosen as:

$$\underset{[3x1]}{\vec{F}} = \underset{[3x6]}{K} \underset{[6x1]}{\vec{X}} \qquad \text{(Equation 2)}$$

where the calibration matrix K is determined using a linear least-squares method over a set of $m \geq 6$ calibration experiments, with singular value decomposition (SVD) of the strain matrix X augmented over m experiments:

$$F = K \cdot U \cdot [diagW] \cdot V^T$$
$$K = F \cdot V \cdot [diagW]^T \cdot U^T \qquad \text{(Equation 3)}$$

With geometric element model simulated data the calibration errors are on the order of 0.01% measured on the force vector norm. The experimental calibration of the sensor is facilitated by the RCM orientation module supporting the RND, which can precisely change the orientation of the needle nozzle so that the sensor may easily be calibrated against a scale. The nozzle is pressed against the scale to various loads (range of 1 – 25N) and RCM angles spanning the motion envelope. The components of the force $\vec{F}$ are determined by projecting the scale reading in the *XYZ* directions according to the inclination angles of the RCM module. The corresponding strain vector $\vec{X}$ is read from the gauges. Experimentally, the sensor was successfully calibrated with less than 5% norm errors.

Gelatin Mockup Design and Construction

A mockup was made embedding stiffer targets within a softer gelatin base contained within a transparent box. The box includes an aluminum frame and glass panes (260mm length × 160mm height × 50mm width). The box was filled with transparent gelatin embedding twelve 10mm diameter × 15mm tall targets so that the needle and the targets can be visually observed during the experiments, as shown in Figure 7. Horizontal thin rubber strings spaced 10mm apart are tied inside the box to show the deformations of the gelatin base. The strings are not attached to the targets.

The targets are made of 300 Bloom gelatin powder (FX Warehouse Inc., Florida) in solution with sorbitol, glycerin, and water (in 3-3-2-1 parts by volume respectively) mixed well and heated to boiling. The solution is poured in a mold, cooled, and extracted. Each target is then briefly submersed in molten wax and cooled to create a thin isolation layer. Twelve equally spaced targets are suspended on needles supported from the top of the box. The stiffness of the targets is approximately 70 points on the Shore OO scale.

The gelatin base is made of the same 300 Bloom powder but 12% concentration in water, mixed and heated to 55–60°C until it becomes clear. The gelatin is then carefully poured into the box until it covers the targets. The wax coat prevents the two gelatin components from mixing because of its higher melting point. When cooled, the needles suspending the targets are withdrawn and gelatin base is added to fill the mockup box. The mockup is then placed in a refrigerator and maintained above freezing temperature overnight. The morning of the experiment, the gel is left to warm at room temperature for 1 hour before needle insertion experiments begin. The stiffness of the gelatin base is on the order of 20 Shore OO.

The above design has been conceptualized and refined starting from an initial experimental setup in which swine kidneys were placed in the gelatin base. However, in this setup experimental measurements were highly dependent on the location of needle insertion within the heterogeneous kidney target. Soft rubber targets were also considered, but high friction between the metallic needle and rubber was unrealistic. The homogeneous gelatin-based targets described above does not include natural tissues but provides a controllable environment for comparing insertions. For simplicity, direct correlation of absolute value mechanical properties of the mockup with natural tissues was not addressed. The mockup simulates relative stiffness differences of pathologic nodules within an organ but is not a model of a specific organ such as kidney, liver, lung, etc. The model was designed to controllably determine the effect of revolving the needle. Eight mockups were made using the same box.

Experimental Setup and Statistical Analysis

Eighteen gauge diamond point (triangular pyramid) needles (Cook DGB-18-15.0) were inserted with the robot through the gelatin towards 90mm deep targets with speeds of 5, 25, and 50 [mm/s]. The second independent variable was the rotation of the needle set at 0, 5, 52 and 101 rpm (speed was selected with a slider control). Rotation at 52 rpm was done both throughout the insertion or only for 5 seconds after reaching the target point, as shown in Table 1. Eleven insertions per each group were performed using 8 mockups and a target was not hit more than twice in order to maintain its bond to the gelatin base.

Axial forces and needle position were recorded every 0.2s during insertion. Digital high-definition video camera recording (Sony HDR-HC1) at 29 frames per second was used for measuring the displacment of the target. The camera was placed at 200 mm from the mockup and the scale was measured from a calibrated background. The frame sequences were processed with Adobe Premiere and Photoshop (Adobe Systems Inc). Images captured provided target displacement measurements with a scale of 14 [pixels/mm]. The shape of the target was superimposed over the images to determine its location, as shown in Figure 8.

Displacements and forces with rotation were compared relative to the control group (no rotation) using Student's *t*-test. A p value of 0.05 or less was considered significant.

Results

Target Displacement

As expected, these controlled and visually observable experiments confirmed that the targets are pushed by the needle when the needle starts to penetrate the target, because the targets are stiffer than the gelatin base (Figure 8 movie). The experiments also showed that the speed of needle insertion and its rotation affects the amount of displacement.

As shown in Figure 9, the displacement of the target is directly related to the speed of insertion and inversely related to revolution. Each point in this graph averages the results of one experiment group (as defined in Table 1) consisting of 11 needle insertions. Without

rotation, the average target displacements are 0.72, 0.83, and 0.96 [mm] for insertion speeds of 5, 25 and 50 [mm/s] respectively. But with rotation (101 rpm) these displacements diminish to 0.44, 0.54, and respectively 0.72 [mm]. Relative to the no-rotation control rotation gives 39.2%, 35.5%, and 25.1% improvements. These changes are statistically significant for the two higher rotary speeds (52 and 101 rpm) in all experiment sets, but not as pronounced for the lower speed (5 rpm).

It should be noted that the experiments above measure the displacement of the target as soon as the insertion stops (pre-revolve). However, a very interesting observation is that a substantial target displacement reduction can be achieved by rotating the needle after insertion (post-revolve). Post-revolve can be done either by continuing the insertion rotation, or starting rotation after insertion.

The bar graph in Figure 10 gathers the no-, pre-, and post-revolve average results of all groups of experiments. For the three speeds of insertion (5, 25, and 50 [mm/s]) the reductions in displacement achieved by post-revolve (52 rpm) with and relative to no pre-revolve are 70.4%, 74.1%, and 76.6%, and are statistically significant for all cases.

Another interesting observation is the time-domain target displacement induced by the post-revolve, as depicted in Figure 11. Post-revolve causes the target that was pushed by the insertion to backup over the needle, thus reducing the initial displacement. The exponential decay approaches asymptotically a remnant targeting error (displacement) within a short time. Based on this observation, five seconds of revolution time was used for all post-revolve experiments described.

Even though post-revolve displacement corrections are similar between no- and pre-revolve experiments, pre-revolve may make a difference in terms of the possible tissue damage that the rotating needle may cause during insertion. Figure 12 shows a detailed view of the needle path in the no-revolve, no pre-revolve with post-revolve, and pre-revolve cases. It appears that rotating the needle during insertion leaves spiral marks on the gelatin path. These are more pronounced with higher revolution and lower insertion speeds (finer pitch). In contrast, post-revolve did not show this pattern. All these experiments used diamond point needles. With bevel points and high speed rotation more tissue damage could possibly occur, but this was not investigated in this study.

Force of Needle Insertion

The force required to insert the needle through the gelatin mass and then the target varies with the depth of needle insertion. For this reason all targets were placed at a constant depth. The axial force applied by the needle immediately after the insertion was evaluated for all experiments. Each bar graph in Figure 13 shows the average force of needle insertion over the 11 insertions in each group of experiments. As for the displacements, the force is higher for faster insertions and for lower revolution speeds. Without rotation, forces are 2.36N, 2.54N, and 3.35N for insertion speeds of 5, 25, and 50 mm/s respectively. With 101 rpm rotation, the respective forces are 1.67N, 1.69N, and 2.88N representing a reduction of 29.3%, 33.7%, and 13.9%.

In the second following the insertion, the above remnant forces show an average reduction of 27.5% without rotation, and can be further reduced by post-revolve to 33.2%, 52.6%, and 58.6% of the original values for the 5, 52, and 101 rpm groups.

Discussion

Percutaneous needle insertion is a commonly performed minimally invasive procedure, and several researchers have developed robotic systems to assist in the procedure. There are simplicity advantages in manually inserting the needle through a guide, keeping the physician in direct control of the needle, and perhaps allowing for simpler regulatory approvals in using these image-guided systems in clinical trials and practice. However, manually inserting the needle reduces the utility of a fully automated system. Automated needle drivers are preferable for certain procedures, including x-ray guidance for reducing radiation exposure, and closed bore MRI scanners where manual access at the isocenter is difficult [21, 29]. Moreover, needle drivers can have additional features such as rotating the needle as presented here.

The revolving needle driver includes two decoupled degrees of freedom for insertion and needle rotation. A new kinematic architecture is used for the needle insertion mechanism that makes it more compact than typical linear stage based drivers. The kinematics are based on a crank hinged-slider rod mechanism that was optimized to render quasi-linear motion. The needle is driven from its head and guided by a nozzle. Two grippers release the needle under a common command. Standard needles of all sizes and types can be used with custom-made adapters. Force sensors measure the force at the nozzle and the force of insertion.

A special gelatin mockup with targets has been developed so that the effect of rotation can be visually observed and measured in a controllable validation setup. Experiments using the RND show that forces and target displacements are reduced by rotation. This is likely achieved by breaking static friction on the barrel of the needle. Displacements and forces were quantified. Both are reduced by slower insertions and faster rotation. Forces and displacements are directly related, but strain-stress linearity could not be validated suggesting that characteristics and effects during needle insertion include components that are beyond elastic and viscous components.

Even though rotating the needle provided improved targeting, when performed during insertion at high revolve/insert velocity ratios, marks were clearly observable along the tract. This raised concerns about possible tissue damage in clinical use, which does not necessarily preclude the use of rotation but should be considered in risk analyses and raises awareness of the type of needle point used and the magnitude of rotation. However, post-revolving the needle proved highly beneficial and did not create tissue damage concerns. Experiments showed that rotating the needle in place after insertion helps the target to backup over the needle, much closer to its intended target point, lowering static insertion displacement errors by as much as 70%. However, post-revolve reduces only target displacements whereas rotating the needle during insertion may provide a straighter trajectory during insertion. This effect has been observed, but represents the object of future experiments.

It is interesting to observe that the conclusion of the study matches and validates the technique that some skilled physicians use manually by rolling the needle back and forth between their fingers. In addition, the study shows that just a few rotations are sufficient to reduce most of the displacement, and that even if prolonged rotation is used these errors are not corrected entirely. To target a stiffer nodule one would also have to practice an overshoot (insert the needle slightly deeper), but anticipating the amount is a very challenging task that will require comprehensive modeling of live tissues. Trial and error correction under direct image guidance remains a solid practical method as it is commonly done, but even so a level of error is still expected. As shown, with rotation target displacement errors are substantially reduced in a simple manner.

Conclusion

An active needle driver is presented including decoupled needle revolving capabilities. The mechanism used for inserting the needle presents an original kinematic structure that makes its body shorter than the needle it handles. The needle insertion study uses a controlled experimental setup to observe how well a needle can target a stiffer lesion of a soft tissue organ, measuring target displacements in the direction of the needle. In-vitro experiments show that the needle always displaces the target. Perfect targeting cannot be achieved without special techniques and/or devices. Targeting error corrections of as much as 70% can be achieved by revolving the needle. In this respect, revolving the needle does not necessarily have to be concomitant with insertion. Post-revolving the needle was also shown to provide similar benefits. The results could have implications for future developments in robotic needle placement.

Supplementary Material

Refer to Web version on PubMed Central for supplementary material.

Acknowledgments

The project described was supported by award number CA094274 from the National Cancer Institute (NCI). The content is solely the responsibility of the authors and does not necessarily represent the official views of the NCI or the National Institutes of Health. Author S.B. is a Recipient of Fellowship Grant from “The American Physicians Fellowship for Medicine in Israel.”

References

1. Cleary K, Melzer A, Watson V, Kronreif G, Stoianovici D. Interventional Robotic Systems: Applications and Technology State-of-the-Art. Minimally Invasive Therapy & Allied Technologies. 2006; Vol.15(2):101–113. PMCID:16754193 http://urobotics.urology.jhu.edu/pub/2006-cleary-mitat.pdf. [PubMed: 16754193]
2. Pollock R, Mozer P, Guzzo TJ, Marx J, Matlaga B, Petrisor D, Vigaru B, Badaan S, Stoianovici D, Allaf ME. Prospects in percutaneous ablative targeting: comparison of a computer-assisted navigation system and the AcuBot Robotic System. Journal of Endourology. 2010 Aug; Vol.24(8): 1269–1272. PMCID:20575701 http://urobotics.urology.jhu.edu/pub/2010-pollock-endourology.pdf. [PubMed: 20575701]
3. Carr JJ, Hemler PF, Halford PW, Freimanis RI, Choplin RH, Chen MY. Stereotactic localization of breast lesions: how it works and methods to improve accuracy. Radiographics. 2001 Mar–Apr; Vol. 21(2):463–473. PMCID:11259709. [PubMed: 11259709]
4. Okamura AM, Simone C, O'Leary MD. Force modeling for needle insertion into soft tissue. IEEE Trans Biomed Eng. 2004 Oct; Vol.51(10):1707–1716. PMCID:15490818. [PubMed: 15490818]
5. Kataoka H, et al. Measurement of tip and friction acting on a needle during penetration. Proceedings of the medical image computing and computer-assisted intervention (MICCAI). 2002:216–223.
6. Matsumiya K, et al. Analysis of forces during robotic needle insertion to human vertebra. Proceedings of the medical image computing and computer-assisted intervention (MICCAI). 2003:271–278.
7. Abolhassani N, Patel R, Moallem M. Needle insertion into soft tissue: a survey. Med Eng Phys. 2007 May; Vol.29(4):413–431. PMCID:16938481. [PubMed: 16938481]
8. Kobayashi Y, Onishi A, Watanabe H, Hoshi T, Kawamura K, Hashizume M, Fujie MG. Development of an integrated needle insertion system with image guidance and deformation simulation. Comput Med Imaging Graph. 2009 Oct 6. PMCID:19815388.
9. Dehghan E, Wen X, Zahiri-Azar R, Marchal M, Salcudean SE. Modeling of needle-tissue interaction using ultrasound-based motion estimation. Med Image Comput Comput Assist Interv. 2007; Vol.10(Pt 1):709–716. PMCID:18051121. [PubMed: 18051121]

10. Abolhassani N, Patel R, Ayazi F. Effects of different insertion methods on reducing needle deflection. Conf Proc IEEE Eng Med Biol Soc. 2007; Vol.2007:491–494. PMCID:18001996. [PubMed: 18001996]
11. Abolhassani N, Patel R, Moallem M. Control of soft tissue deformation during robotic needle insertion. Minim Invasive Ther Allied Technol. 2006; Vol.15(3):165–176. PMCID:16785183. [PubMed: 16785183]
12. Podder TK, Clark DP, Fuller D, Sherman J, Ng WS, Liao L, Rubens DJ, Strang JG, Messing EM, Zhang YD, Yu Y. Effects of velocity modulation during surgical needle insertion. Conf Proc IEEE Eng Med Biol Soc. 2005; Vol.6:5766–5770. PMCID:17281568. [PubMed: 17281568]
13. Meltsner MA, Ferrier NJ, Thomadsen BR. Observations on rotating needle insertions using a brachytherapy robot. Phys Med Biol. 2007 Oct 7; Vol.52(19):6027–6037. PMCID:17881817. [PubMed: 17881817]
14. DiMaio SP, Salcudean SE. Needle steering and motion planning in soft tissues. IEEE Trans Biomed Eng. 2005 Jun; Vol.52(6):965–974. PMCID:15977726. [PubMed: 15977726]
15. Alterovitz R, Branicky M, Goldberg K. Motion Planning Under Uncertainty for Image-guided Medical Needle Steering. Int J Rob Res. 2008; Vol.27(11–12):1361–1374. PMCID:19890445. [PubMed: 19890445]
16. Glozman D, Shoham M. Flexible needle steering for percutaneous therapies. Comput Aided Surg. 2006 Jul; Vol.11(4):194–201. PMCID:17060077. [PubMed: 17060077]
17. Ding J, Stoianovici D, Petrisor D, Mozer P, Avila R, Ibanez L, Turner W, Yankelvitz D, Wilson E, Banovac F, Cleary K. Medical needle steering for lung biopsy: Experimental results in tissue phantoms using a robotic needle driver. IEEE International Conference on BioInformatics and BioEngineering. 2008 http://urobotics.urology.jhu.edu/pub/2008-ding-bibe.pdf.
18. Lagerburg V, Moerland MA, Konings MK, van de Vosse RE, Lagendijk JJ, Battermann JJ. Development of a tapping device: a new needle insertion method for prostate brachytherapy. Phys Med Biol. 2006 Feb 21; Vol.51(4):891–902. PMCID:16467585. [PubMed: 16467585]
19. Muntener M, Patriciu A, Petrisor D, Mazilu D, Kavoussi L, Cleary K, Stoianovici D. Magnetic Resonance Imaging Compatible Robotic System for Fully Automated Brachytherapy Seed Placement. Urology. 2006 Dec; Vol.68(6):1313–1317. http://urobotics.urology.jhu.edu/pub/2006-muntener-urology.pdf. [PubMed: 17169653]
20. Patriciu A, Petrisor D, Muntener M, Mazilu D, Schar M, Stoianovici D. Automatic Brachytherapy Seed Placement under MRI Guidance. IEEE Transactions on Biomedical Engineering. 2007 Aug; Vol.54(8):1499–1506. PMCID:17694871 http://urobotics.urology.jhu.edu/pub/2007-patriciu-tbme.pdf. [PubMed: 17694871]
21. Stoianovici D, Song D, Petrisor D, Ursu D, Mazilu D, Muntener M, Schar M, Patriciu A. “MRI Stealth” Robot for Prostate Interventions. Minimally Invasive Therapy & Allied Technologies. 2007; Vol.16(4):241–248. PMCID:17763098 http://urobotics.urology.jhu.edu/pub/2007-stoianovici-mitat.pdf. [PubMed: 17763098]
22. Stoianovici D, Cleary K, Patriciu A, Mazilu D, Stanimir A, Craciunoiu N, Watson V, Kavoussi LR. AcuBot: A Robot for Radiological Interventions. IEEE Transactions on Robotics and Automation. 2003 Oct; Vol.19(5):926–930. http://urology.jhu.edu/urobotics/pub/2003-stoianovici-ieeetra.pdf.
23. Zangos S, Herzog C, Eichler K, Hammerstingl R, Lukoschek A, Guthmann S, Gutmann B, Schoepf UJ, Costello P, Vogl TJ. MR-compatible assistance system for punction in a high-field system: device and feasibility of transgluteal biopsies of the prostate gland. Eur Radiol. 2007 Apr; Vol.17(4):1118–1124. PMCID:17031454. [PubMed: 17031454]
24. Mozer P, Troccaz J, Stoianovici D. Urologic robots and future directions. Current Opinion in Urology. 2009 Jan; Vol.19(1):114–119. PMCID:19057227 http://urobotics.urology.jhu.edu/pub/2009-mozer-cou.pdf. [PubMed: 19057227]
25. Podder TK, Ng WS, Yu Y. Multi-channel robotic system for prostate brachytherapy. Conf Proc IEEE Eng Med Biol Soc. 2007; Vol.2007:1233–1236. PMCID:18002186. [PubMed: 18002186]
26. Mozer P, Partin AW, Stoianovici D. Robotic Image-Guided Needle Interventions of the Prostate. Reviews in Urology. 2009 Winter;Vol.11(1):7–15. PMCID:19390670 http://urobotics.urology.jhu.edu/pub/2009-mozer-revurol.pdf. [PubMed: 19390670]

27. Stoianovici D, Whitcomb LL, Anderson JH, Taylor RH, Kavoussi LR. A modular surgical robotic system for image guided percutaneous procedures. Lecture Notes in Computer Science. 1998; Vol. 1496:404–410. http://urology.jhu.edu/urobotics/pub/1998-stoianovici-miccai.pdf.

28. Shah S, Kapoor A, Ding J, Guion P, Petrisor D, Karanian J, Pritchard W, Stoianovici D, Wood B, Cleary K. Robotically Assisted Needle Driver: Evaluation of Safety Release, Force Profiles, and Needle Spin in a Swine Abdominal Model. International Journal of Computer Assisted Radiology and Surgery. 2008; Vol.3:173–179. http://urobotics.urology.jhu.edu/pub/2008-shah-ijcars.pdf.

29. Stoianovici D, Patriciu A, Mazilu D, Petrisor D, Kavoussi L. A New Type of Motor: Pneumatic Step Motor. IEEE/ASME Transactions on Mechatronics. 2007 Feb; Vol.12(1):98–106. *2008 Best Paper Award of the Journal*. http://urobotics.urology.jhu.edu/pub/2007-stoianovici-tmech.pdf. [PubMed: 21528106]

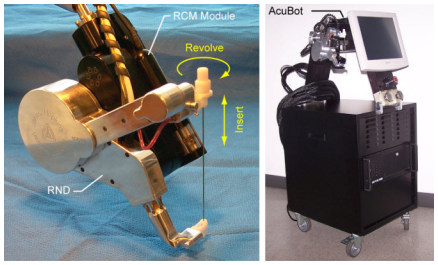

Figure 1.
Revolving Needle Driver supported by the RCM orientation module (left) and the AcuBot robot with its control cabinet (right)

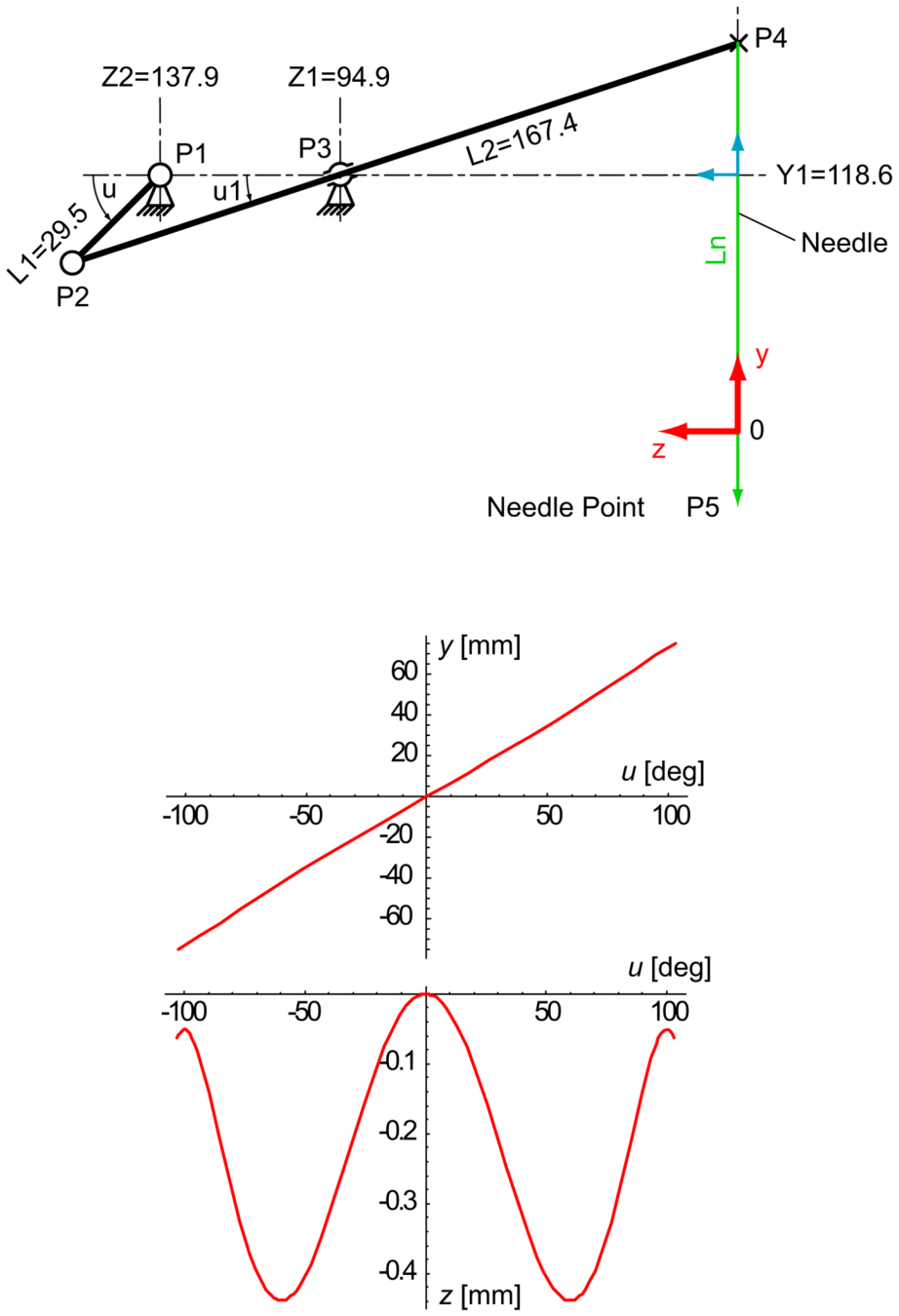

Figure 2.
Kinematic diagram of the needle insertion mechanism (left). The y and z coordinates of the needle point as a function of the driving crank angle u (right).

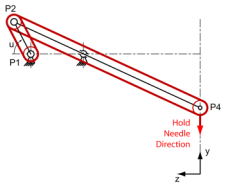

Figure 3.
Parallel motion mechanism used over the needle insertion mechanism to maintain the direction of the needle during insertion.

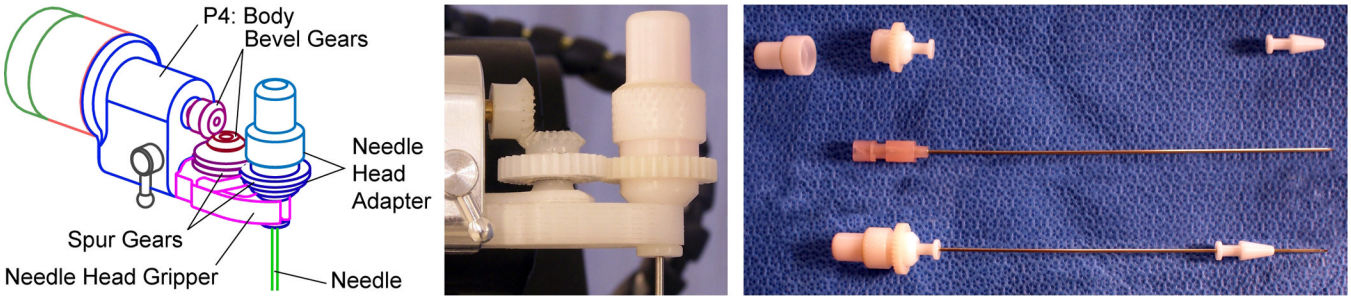

Figure 4.
Needle head gripper assembly with rotation mechanism and needle adapters with gear for revolving.

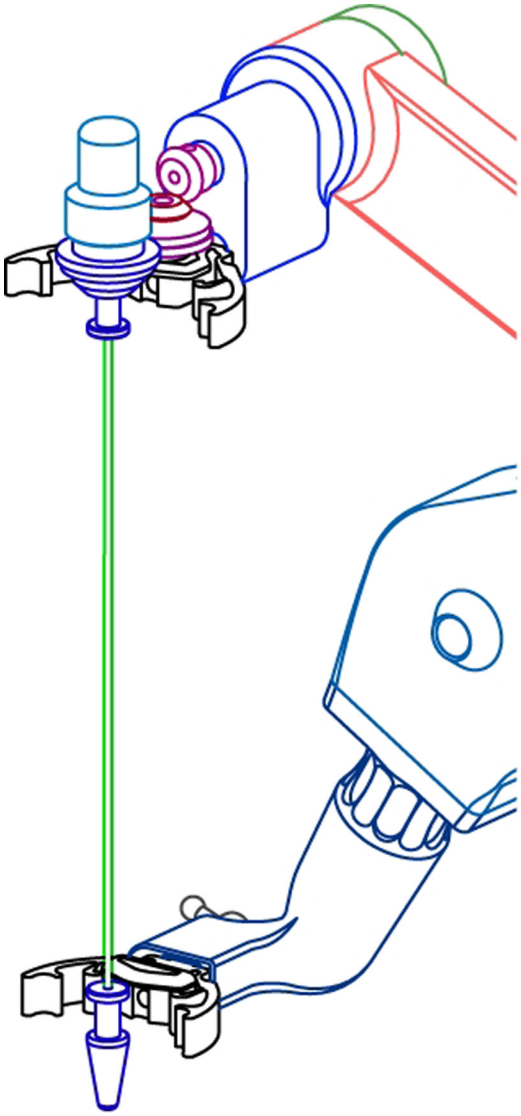

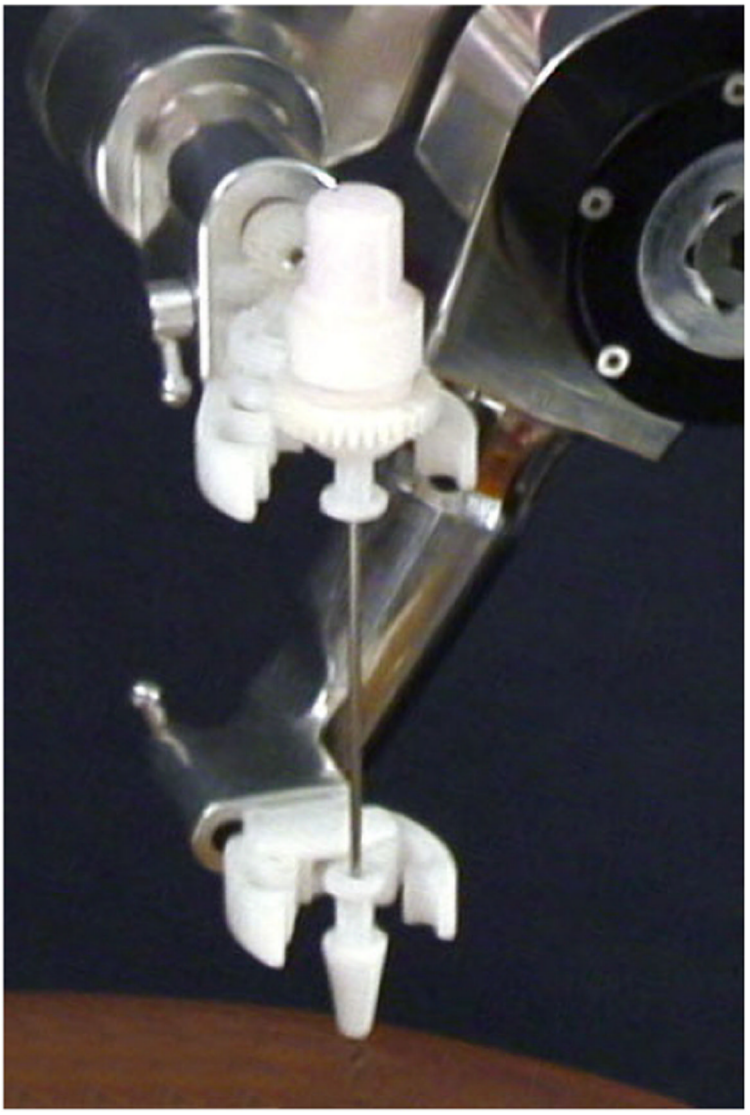

Figure 5.
Grippers swing aside to release needle under computer control.

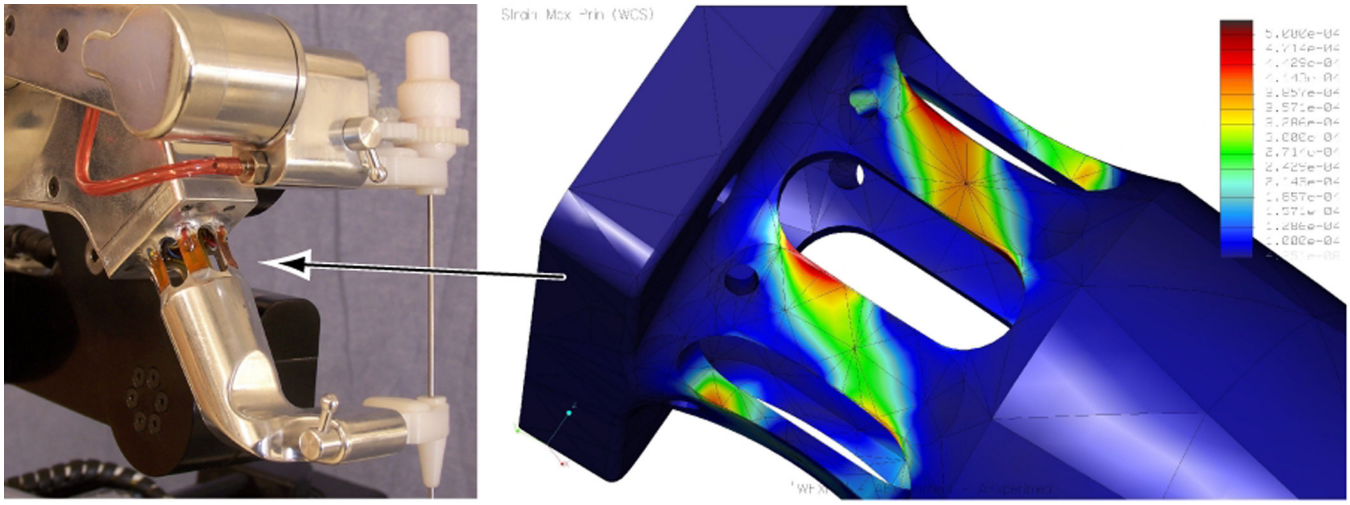

Figure 6.
Experimental Setup: AcuBot robot with RND and translucent gelatin box (left), needle and targets (right)

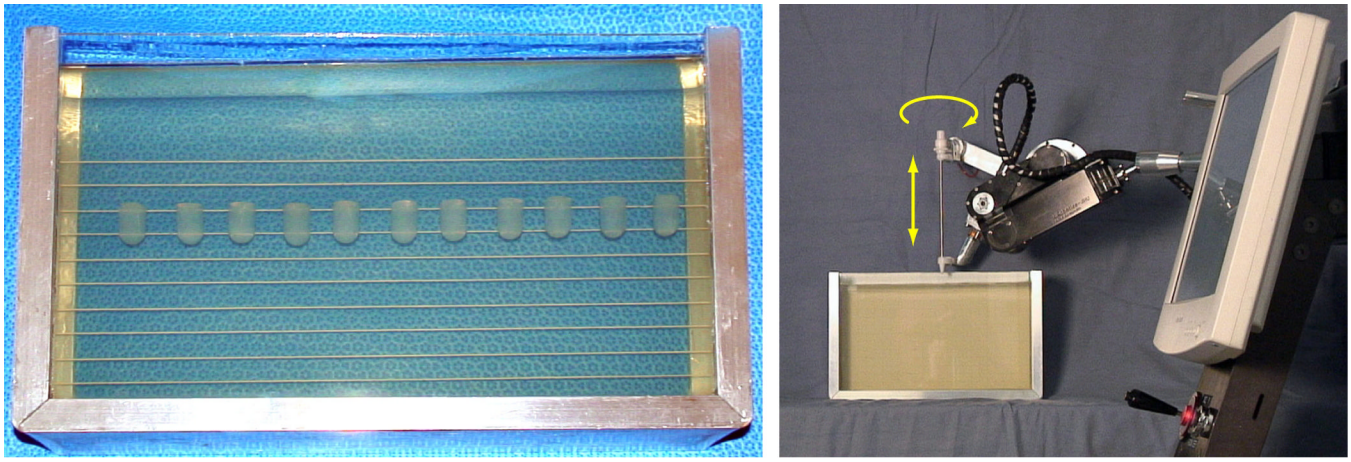

Figure 7.
Built in custom nozzle force sensor and geometric element model design

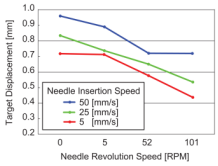

Figure 8.
Target displacement vs. needle rotation speed for three speeds of needle insertion.

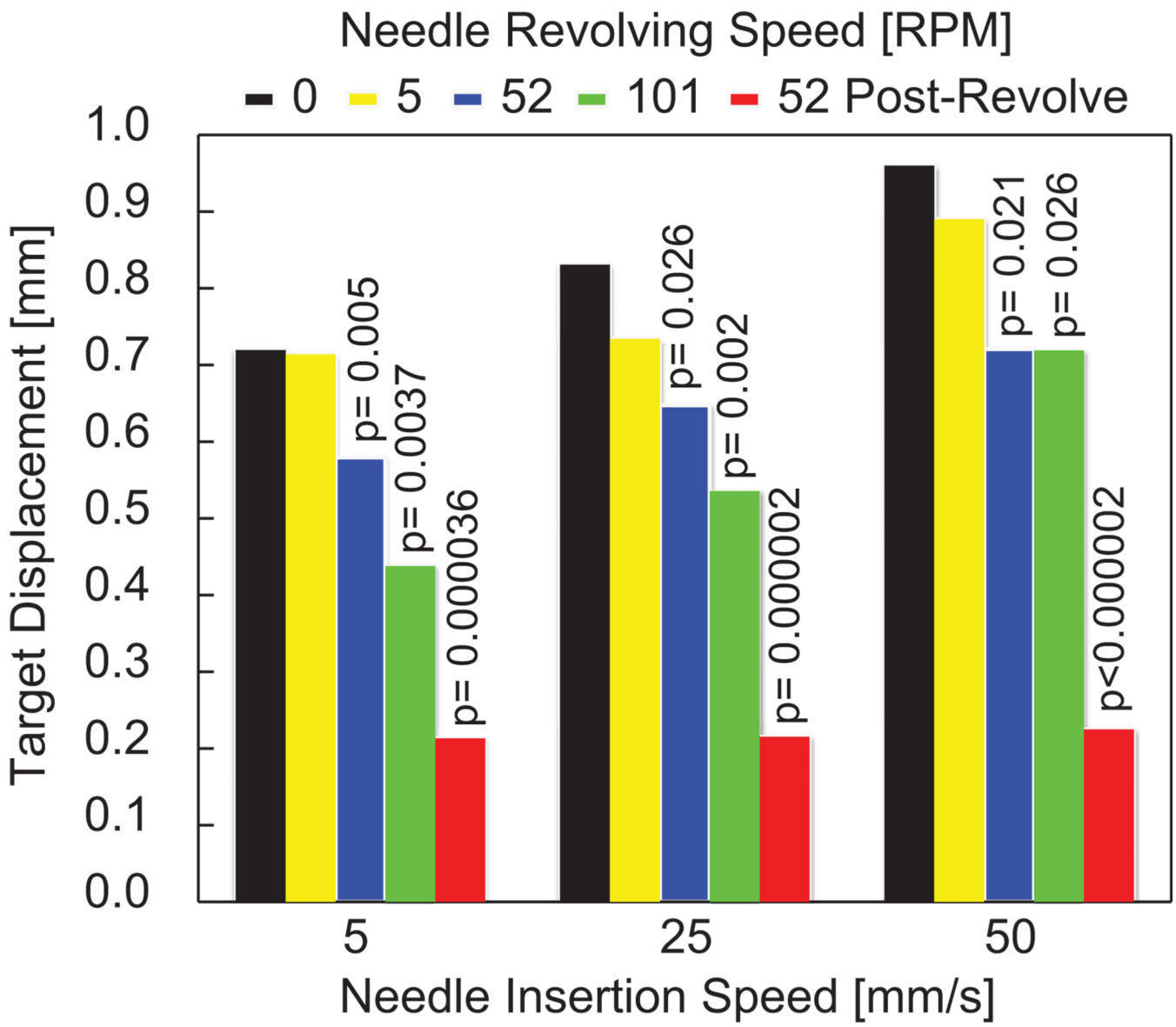

Figure 9.
Target displacements with no-revolve, when rotating while inserting (pre-revolve), and rotating after the insertion (post-revolve). The confidence in the lower results relative to the no-revolve control is shown by the probability values p.

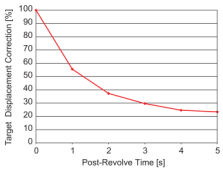

Figure 10.
Target displacement during 5s post-revolve (52 rpm) shows that the target moves backward over the needle reducing targeting errors.

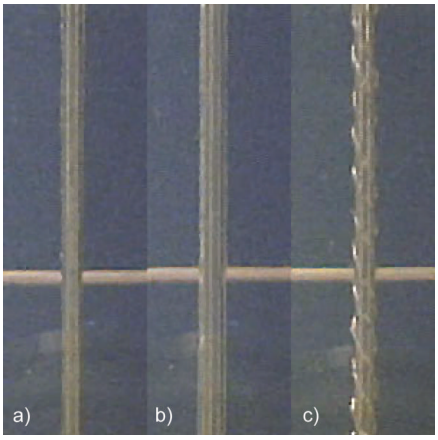

Figure 11.
Three images of the needle shaft inserted in the gelatin with: a) no pre-revolve showing no apparent gelatin marks, b) no pre-revolve but post-revolve showing no apparent gelatin marks, and c) pre-revolve (5 mm/s and 52 rpm) showing helical marks in the gelatin.

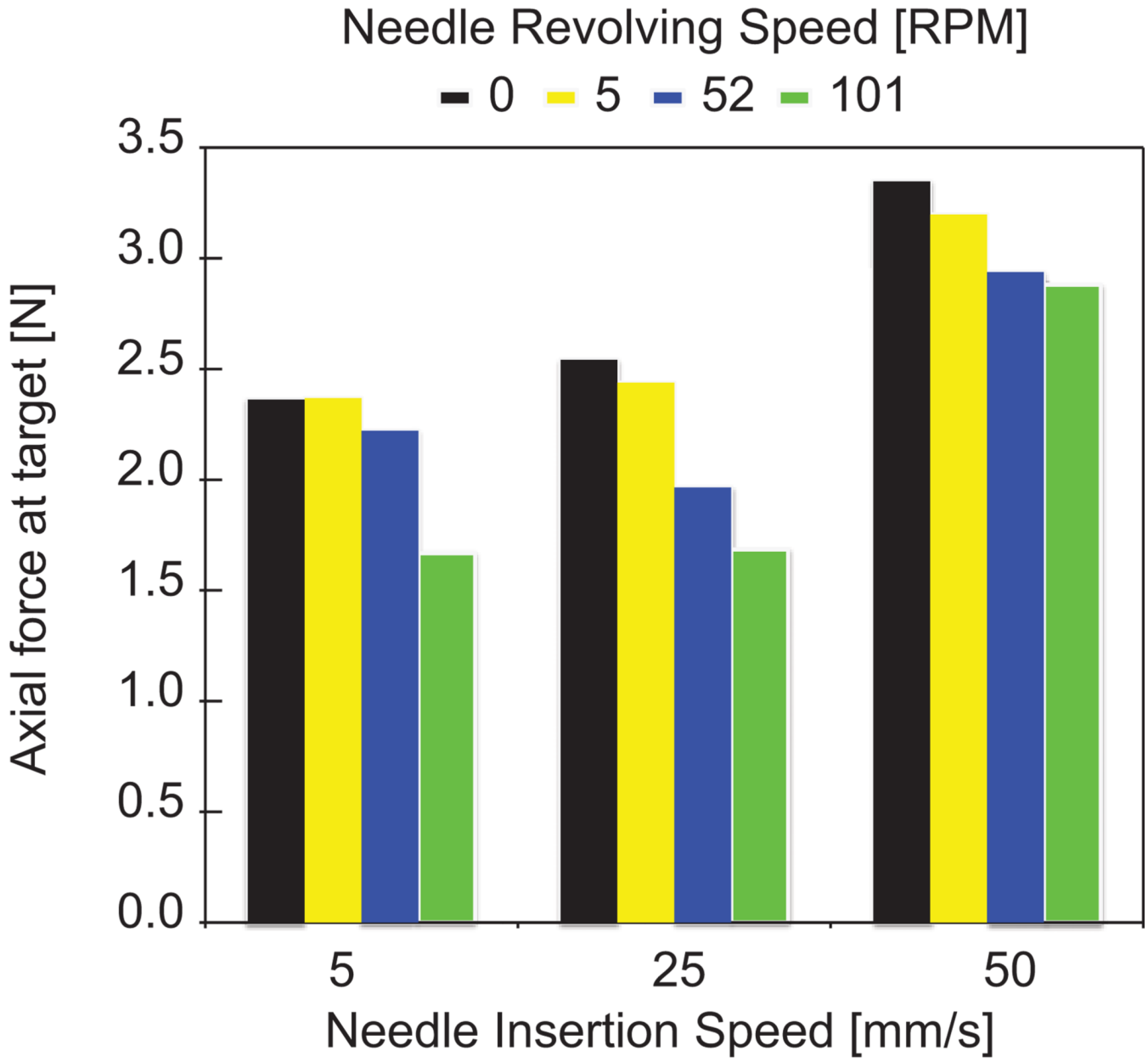

Figure 12.
Axial needle force measured at target point vs. needle insertion speed for several needle revolution speeds.

Table 1

Experiment Design: 15 groups, 5 groups per insertion speed, 11 replicated tests per group

Experiment group	Insertion Speed [mm/s]	Rotation Speed [rpm]	Rotation Method
1	5	0	No Rotation (Control)
2		5	Rotate throughout insertion (pre-Revolve)
3		52	
4		101	
5		52	Rotate after reaching target point (post-Revolve)
6	25	0	No Rotation (Control)
7		5	Rotate throughout insertion (pre-Revolve)
8		52	
9		101	
10		52	Rotate after reaching target point (post-Revolve)
11	50	0	No Rotation (Control)
12		5	Rotate throughout insertion (pre-Revolve)
13		52	
14		101	
15		52	Rotate after reaching target point (post-Revolve)